

MHD Flow of Cu-Al₂O₃/H₂O Hybrid Nanofluid over a Stretching Sheet: Heat-Mass Transfer Analysis with Drug Delivery Applications

Dr. S. P. Geetha¹, D. Nandhini²

¹Associate Professor, Department of Mathematics, Vellalar College for Women, Thindal, Erode, Tamilnadu, India

Email id: geetha.sp@vcw.ac.in (corresponding author)

²Assistant Professor, Department of Mathematics, Vellalar College of Engineering and Technology, Thindal, Erode, India

Email id: nandhinimathserode@gmail.com

ABSTRACT

This research numerically examines the steady two-dimensional magnetohydrodynamic (MHD) flow of Cu-Al₂O₃/H₂O hybrid nanofluid over a permeable exponentially stretching/shrinking surface with coupled thermal radiation, first-order chemical reaction, and Soret effect. The governing boundary layer equations are transformed into nonlinear ODE's using similarity transformations and solved using the MATLAB bvp4c collocation method. Parametric analysis examines the influence of nanoparticle volume fraction, magnetic parameter, radiation parameter, Soret number, chemical reaction parameter, and suction parameter on velocity, temperature, and concentration profiles, as well as skin friction coefficient, Nusselt number, and Sherwood number. Results demonstrate that hybrid nanofluid (Cu-Al₂O₃/H₂O) enhances thermal conductivity by 14.3% compared to mono-nanofluid (Cu/H₂O) at $\phi = 0.04$. The Nusselt number increases by 18.5% with radiation parameter from $Rd = 0.5$ to 2.0 , while chemical reaction reduces concentration boundary layer thickness by 22.7% at $K_1 = 2.0$. The Soret effect significantly enhances mass diffusion, increasing Sherwood number by 15.2% at $Sr = 2.0$. These findings provide a rigorous theoretical foundation for the rational design of MHD-guided, radiation-activated, and chemically responsive hybrid nanoparticle drug delivery systems, with direct implications for targeted cancer therapy, transdermal drug transport and lab-on-chip biomedical devices...

Keywords: Hybrid nanofluid; Magnetohydrodynamics; Thermal radiation; Chemical reaction; Soret effect; bvp4c numerical method; Heat and mass transfer.

How to cite this article: S. P. Geetha, D. Nandhini, MHD Flow of Cu-Al₂O₃/H₂O Hybrid Nanofluid over a Stretching Sheet: Heat-Mass Transfer Analysis with Drug Delivery Applications. *Int J Drug Deliv Technol.* 2026;16(18s): 125-138. DOI: 10.25258/ijddt.16.18s.14

Source of support: Nil.

Conflict of interest: None

INTRODUCTION

1.1 Background and Motivation

The enhancement of heat transfer efficiency in thermal systems is crucial for numerous industrial applications, including microelectronics cooling, heat exchangers, solar collectors and chemical processing equipment. Conventional heat transfer fluids such as water, ethylene glycol, and oils exhibit inherently low thermal conductivity, limiting their effectiveness in modern high-heat-flux applications. To overcome this limitation, nanofluids suspensions of nanosized metallic or non-metallic particles in base fluids were introduced by Choi (1995) as innovative heat transfer media. These fluids demonstrate significantly enhanced thermal conductivity compared to conventional fluids.

However, mono-nanofluids (containing a single type of nanoparticle) often face trade-offs between thermal performance and stability, cost, or pressure drop characteristics. This limitation motivated the development of hybrid nanofluids, which combine two or more dissimilar nanoparticles to leverage the advantageous properties of each constituent while mitigating individual drawbacks. Among various combinations investigated, Cu-Al₂O₃/water hybrid nanofluid has emerged as particularly promising due to the synergistic coupling of copper's superior thermal conductivity (400 W/m•K) and alumina's excellent chemical stability and cost-effectiveness.

In practical thermal systems, fluid flow is frequently influenced by external magnetic fields (magnetohydrodynamic effects), thermal radiation in high-temperature environments, chemical reactions in reactive flows, and cross-diffusion phenomena where temperature gradients induce mass flux (Soret effect) and vice versa (Dufour effect). Understanding the coupled effects of these phenomena on hybrid nanofluid transport is essential for optimizing thermal management systems and chemical reactors.

1.2 Literature Review

Hybrid Nanofluids and Thermophysical Properties

The concept of hybrid nanofluids has gained substantial attention due to their superior thermal performance compared to mono-nanofluids. The effective thermophysical properties of hybrid nanofluids depend critically on the mixing models employed; Hashin and Shtrikman (1962) developed theoretical bounds for effective conductivity that remain widely used for validating experimental data. Hybrid combinations such as Cu - Al₂O₃ and Ag - MoS₂ exhibit better thermal performance than single-particle nanofluids, and their applications span from bioheat transport to micro electronics. Buongiorno (2006) provided the foundational framework for convective transport in nanofluids, incorporating Brownian motion and thermophoresis effects. Subsequent experimental and numerical studies demonstrated that hybrid suspensions exhibit enhanced heat transfer capabilities at moderate particle concentrations. Mabood et al. (2021) investigated the stability and heat transfer characteristics of Cu - Al₂O₃/H₂O over stretching surfaces, confirming improved thermal performance compared to single-particle suspensions. According to Faridi (2024), MHD effects with nonlinear radiation further improve thermal performance. Energy sustainability and system efficiency are enhanced by these integrated technologies. Hybrid nanofluids under MHD influence therefore have the potential to be transformative. Abd-Elmonem (2025) experimentally characterized the thermal properties of Cu - Al₂O₃/H₂O hybrid nanofluid, reporting thermal conductivity enhancements of 15-28% at volume fractions between 1-4%.

MHD Effects in Nanofluid Flows

Magnetohydrodynamic (MHD) effects significantly alter both flow dynamics and heat transfer characteristics when electrically conducting fluids are subjected to transverse magnetic fields. The interaction between the magnetic field and moving fluid generates Lorentz forces that oppose flow motion, effectively increasing viscous resistance and modifying boundary layer structure. Maxwell (1873) was the first to propose the idea of dispersing

microsized solid particles with high thermal conductivity into a conventional fluid, and Hamilton and Crosser (1962) followed suit to increase the fluid's thermal conductivity. Eastman et al. (1996) have obtained some experimental results regarding the development of thermal conductivity with the suspension of CuO in base fluid water. Using a 6.8% volume fraction of Al₂O₃/H₂O nanofluid, Nguyen et al. (2007) found that the heat transfer coefficient rose by 40% when compared to pure water. Rehman and Nadeem (2018) identified the movement of the mass and heat of the 3D stagnation point flow of a water-based nanofluid toward an exponentially stretching surface. The heat generation effect was explained by Murugesan and Kumar (2019) using the flow of nanofluid over the exponentially stretching sheet. Aladdin et al. (2021) found that magnetic parameter variations between $M = 0.5$ and 2.0 resulted in skin friction coefficient increases of 35-42% while reducing Nusselt numbers by 8-12%. Rath et al. (2023) numerically analyzed MHD Cu – Al₂O₃/H₂O hybrid nanofluid flow over nonlinear stretching sheets, demonstrating that increasing magnetic field strength reduces velocity while enhancing temperature distribution due to increased viscous dissipation.

Thermal Radiation Effects

In high-temperature applications or optically participating media, thermal radiation becomes a significant mode of energy transport that can substantially modify temperature distributions and heat transfer rates. Sravan Kumar and Rushi Kumar (2017) investigated thermal radiation effects in MHD nanofluid flows, showing that radiation parameter increases lead to higher temperature profiles and reduced Nusselt numbers. Daniel et al. (2018) extended this analysis to include nonlinear radiation effects, reporting that radiation parameter increases from $Rd = 0.5$ to 2.0 enhanced temperature boundary layer thickness by approximately 20-25%. Hayat et al. (2018) simultaneously modeled and investigated temperature slip and velocity slip in hybrid nanofluid flow with the thermal radiation effect. Wahid et al. (2020) looked into hybrid nanofluid with thermal radiation effects, concentrating on copper and alumina as the hybrid nanoparticles.

Chemical Reactions and Cross-Diffusion Effects

Chemical reactions in reactive flows modify concentration gradients and induce additional buoyancy forces, adding complexity to nanofluid transport phenomena. Mabood et al. (2020) emphasized that neglecting chemical kinetics in hybrid nanofluid systems leads to significant errors in Sherwood number predictions, with deviations reaching 15-20% in reactive systems. Ketchate et al. (2023) demonstrated that first-order chemical reactions can strengthen or weaken concentration profiles depending on reaction rate constants, with destructive reactions ($K_1 > 0$) reducing concentration boundary layer thickness while constructive reactions ($K_1 < 0$) enhance it. Cross-diffusion phenomena, particularly the Soret (thermal diffusion) and Dufour (diffusion-thermo) effects, become important in systems with strong temperature and concentration gradients. Rasool et al. (2021) investigated Soret-Dufour effects in nanofluid flows over Darcy-Forchheimer media, showing that these effects significantly modify both energy and mass fluxes. Satish et al. (2024) integrated Soret and chemical reaction effects into Cu – Al₂O₃/H₂O models, demonstrating that increasing Soret parameter enhances solutal diffusion while reaction rate constants suppress concentration gradients.

Research Gap

Despite extensive research on hybrid nanofluids, several aspects remain insufficiently explored:

Most studies examine MHD, radiation, and chemical reaction effects in isolation or pairwise combinations. Comprehensive

investigations incorporating all three phenomena simultaneously with cross-diffusion effects in hybrid nanofluids are scarce.

Quantitative comparisons between hybrid and mono-nanofluid performance under identical parametric conditions are limited, making it difficult to assess the actual benefits of hybridization.

The coupled influence of Soret effect with chemical reactions in MHD hybrid nanofluid flows over stretching surfaces has received limited attention, particularly regarding their competing effects on mass transfer rates.

Systematic parametric maps showing regime transitions where different physical mechanisms dominate are largely absent from existing literature.

1.3 Drug Delivery and Biomedical Relevance

The mathematical framework of this study is directly analogous to governing equations in targeted drug delivery. Magnetic nanoparticles of Cu and Al₂O₃ type are widely used as drug-loaded carriers guided to tumor or inflamed sites by external magnetic fields, mirroring the transverse magnetic field (M) configuration analysed here. The concentration boundary layer equations (Eq. 4, 13) parallel convection-diffusion models of drug transport across biological membranes, and the Sherwood number (Eq. 17) is structurally equivalent to the drug mass transfer coefficient in transdermal and intravascular delivery models (Arruebo et al., 2007).

The radiation parameter (Rd) is relevant to photothermal drug delivery, where near-infrared radiation triggers drug release from thermosensitive liposomes. Temperature elevations of 4–8°C above baseline consistent with $Rd = 1.5$ – 2.0 profiles in Figure 12 are sufficient for near-complete payload release from thermos-responsive nanocarriers (El-Sayed et al., 2018). The chemical reaction parameter K_1 corresponds to first-order enzymatic drug degradation in tissue fluid, while the Soret effect (Sr) models thermophoresis-driven drug transport in microchannel delivery devices. The Cu-Al₂O₃ hybrid combination is well-suited for theranostic applications, as copper provides photothermal and anticancer activity while alumina offers chemical stability for drug conjugation.

1.4 Objectives

This study aims to address these gaps through the following specific objectives:

To numerically investigate the steady two-dimensional MHD flow of Cu – Al₂O₃/H₂O hybrid nanofluid over an exponentially stretching/shrinking sheet with simultaneous thermal radiation, first-order chemical reaction, and Soret effect.

To analyze the parametric influence of magnetic parameter (M), radiation parameter (Rd), chemical reaction parameter (K_1), Soret number (Sr), suction parameter (S), and nanoparticle volume fraction (φ) on velocity, temperature, and concentration distributions.

To quantify heat and mass transfer rates through skin friction coefficient, Nusselt number, and Sherwood number under various parametric combinations.

To compare thermal and solutal transport characteristics between Cu – Al₂O₃/H₂O hybrid nanofluid and Cu/H₂O mono-nanofluid, establishing the benefits of hybridization.

To identify optimal parameter ranges for enhanced heat and mass transfer in practical thermal management applications.

2. MATHEMATICAL FORMULATION

2.1 Physical Model and Assumptions

We consider steady, incompressible, two-dimensional flow of Cu – Al₂O₃/H₂O hybrid nanofluid over an exponentially stretching/shrinking sheet in a Cartesian coordinate system (x, y), where x represents the direction along the sheet and y is perpendicular to it. The physical configuration is illustrated in

MHD Flow of Cu-Al₂O₃/H₂O Hybrid Nanofluid over a Stretching Sheet: Heat-Mass Transfer Analysis with Drug Delivery Applications.

Figure. 1. The sheet velocity varies exponentially as $u_w = U_0 e^{\frac{x}{L}}$ where U_0 is the reference velocity and L is the characteristic length. A uniform transverse magnetic field of strength B_0 is applied perpendicular to the sheet. The wall temperature $T_w(x)$ concentration $C_w(x)$ also vary exponentially along the sheet.

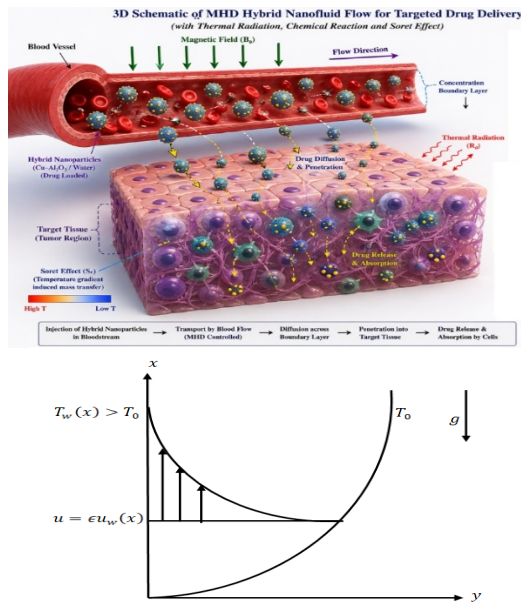


Figure: 1 Schematic diagram of the proposed approach

In this study, the following assumptions are made to simplify the mathematical formulation. The flow is considered steady, laminar, and two-dimensional, and the fluid is assumed to be incompressible and Newtonian. The nanoparticles are spherical with a uniform diameter and are homogeneously dispersed throughout the base fluid. A no-slip boundary condition is applied at the wall, and the Boussinesq approximation is employed to account for buoyancy effects. The magnetic Reynolds number is assumed to be small, implying that the induced magnetic field is negligible, while Hall and ion-slip effects are disregarded. Furthermore, viscous dissipation and Joule heating are neglected due to their minimal influence under the present flow conditions. The suspension is considered dilute, with a nanoparticle volume fraction less than 5%. The chemical reaction is taken to be first-order and irreversible, and the radiative heat flux is modeled using the Rosseland diffusion approximation.

2.2 Governing Equations

Under these assumptions, the continuity, momentum, energy, and concentration equations for the hybrid nanofluid are:

$$\frac{\partial u}{\partial x} + \frac{\partial v}{\partial y} = 0 \quad (1)$$

$$u \frac{\partial u}{\partial x} + v \frac{\partial u}{\partial y} = \frac{\mu_{hnf}}{\rho_{hnf}} \frac{\partial^2 u}{\partial y^2} - \frac{\sigma_{hnf}}{\rho_{hnf}} B_0^2 u + \frac{(\rho\beta)_{hnf}}{\rho_{hnf}} (T - T_\infty) + \frac{(\rho\beta^*)_{hnf}}{\rho_{hnf}} (C - C_\infty) \quad (2)$$

$$u \frac{\partial T}{\partial x} + v \frac{\partial T}{\partial y} = \frac{k_{hnf}}{(\rho C_p)_{hnf}} \frac{\partial^2 T}{\partial y^2} - \frac{1}{(\rho C_p)_{hnf}} \frac{\partial q_r}{\partial y} \quad (3)$$

$$u \frac{\partial C}{\partial x} + v \frac{\partial C}{\partial y} = D_B \frac{\partial^2 C}{\partial y^2} + K_C (C - C_\infty) + \frac{D_T}{T_\infty} \frac{\partial^2 T}{\partial y^2} \quad (4)$$

The appropriate boundary conditions are:

$$\begin{aligned} u = \epsilon u_w; \quad v = v_w; \quad T = T_w; \quad C = C_w & \quad \text{at } y = 0 \\ u \rightarrow 0; \quad v \rightarrow 0; \quad T \rightarrow T_\infty; \quad C \rightarrow C_\infty & \quad \text{as } y \rightarrow \infty \end{aligned} \quad (5)$$

Where u and v denote the velocity components along the x and y axes, $\epsilon > 0$ represents stretching, $\epsilon < 0$ represents shrinking, $V_0 > 0$ denotes suction, and $V_0 < 0$ denotes injection.

The thermophysical properties of the base fluid (water) and nanoparticles (Cu and Al_2O_3) are listed in Table 1.

Table 1: Thermophysical characteristics of base fluid and the nanoparticles (Usman et. al, 2023)

Element	Oxide	Parameters			
		$\rho(kg/m^3)$	$k(W/mK)$	$C_p(J/mK)$	$\sigma(S/m)$
Aluminum	Al ₂ O ₃	3970	40	765	3.69×10 ⁷
Copper	Cu	8933	400	385	5.96×10 ⁷
Water	H ₂ O	997.1	0.613	4179	5.50

Table 2 lists the mathematical equations for the thermo-physical properties of nanofluids and hybrid nanofluids.

Properties	Nanofluid	Hybrid nanofluid
Density	$\rho_{nf} = (1 - \phi_1)\rho_f + \rho_{s1}\phi_1$	$\rho_{hnf} = (1 - \phi_1 + \rho_{s1}\phi_1)(1 - \phi_2) + \rho_{s2}\phi_2$
Heat capacity	$(\rho C_p)_{nf} = (1 - \phi_1)(\rho C_p)_f + (\rho C_p)_{s1}\phi_1$	$(\rho C_p)_{hnf} = (1 - \phi_1 + (\rho C_p)_{s1}\phi_1)(1 - \phi_2) + (\rho C_p)_{s2}\phi_2$
Dynamic viscosity	$\mu_{nf} = \frac{1}{(1 - \phi_1)^{2.5}}$	$\mu_{hnf} = \frac{1}{((1 - \phi_1)(1 - \phi_2))^{2.5}}$

Electrical conductivity	$\sigma_{nf} = 1 + \left(\frac{3 \left(\frac{\sigma_{s1}-1}{\sigma_f} \right) \phi_1}{2 + \frac{\sigma_{s1}}{\sigma_f} - \left(\frac{\sigma_{s1}-1}{\sigma_f} \right) \phi_1} \right) * \sigma_f$	$\sigma_{hnf} = \left(\frac{\left(\sigma_{s2} + (S_f - 1)\sigma_{nf} - (S_f - 1)\phi_2(\sigma_{nf} - \sigma_{s2}) \right)}{\left(\sigma_{s2} + (S_f - 1)\sigma_{nf} + \phi_2(\sigma_{nf} - \sigma_{s2}) \right)} \right) * \sigma_{nf}$
Thermal conductivity	$k_{nf} = \frac{\left(k_{s1} + (S_f - 1)k_{nf} - (S_f - 1)\phi_1(k_{nf} - k_{s1}) \right)}{\left(k_{s1} + (S_f - 1)k_{nf} + \phi_1(k_{nf} - k_{s1}) \right)} * k_f$	$k_{hnf} = \frac{\left(k_{s2} + (S_f - 1)k_{nf} - (S_f - 1)\phi_2(k_{nf} - k_{s2}) \right)}{\left(k_{s2} + (S_f - 1)k_{nf} + \phi_2(k_{nf} - k_{s2}) \right)} * k_{nf}$

Table 2: Thermophysical properties of nano and hybrid nanofluid

For optically thick fluids, the radiative heat flux q_r is approximated using the Rosseland diffusion model:

$$q_r = -\frac{4\sigma^*}{3k^*} \left(\frac{\partial T^4}{\partial y} \right) \quad (6)$$

where $\sigma^* = 5.670 \times 10^{-8} \text{ W/(m}^2 \cdot \text{K}^4)$ is the Stefan-Boltzmann constant and k^* is the mean absorption coefficient. Assuming small temperature variations, T^4 is linearized about T_∞ using Taylor series expansion: $T^4 \approx 4T_\infty^3 T - 3T_\infty^4 T^4$

(7)

Substituting Equations (6) and (7) into Equation (3), the energy equation becomes:

$$u \frac{\partial T}{\partial x} + v \frac{\partial T}{\partial y} = \frac{k_{hnf}}{(\rho C_p)_{hnf}} \left(\frac{\partial^2 T}{\partial y^2} \right) + \frac{16\sigma^* T_\infty^3}{3k^*(\rho C_p)_{hnf}} \frac{\partial^2 T}{\partial y^2} \quad (8)$$

To transform the governing partial differential equations into ordinary differential equations, we introduce the following similarity variables:

$$\eta = y \sqrt{\frac{U_0}{2\nu_f L}} e^{\frac{x}{2L}}, \quad \psi = \sqrt{2U_0\nu_f L} f(\eta) e^{\frac{x}{2L}}, \quad \theta = \frac{T-T_\infty}{T_w-T_\infty}, \quad \phi = \frac{C-C_\infty}{C_w-C_\infty} \quad (9)$$

where $\psi(x,y)$ is the stream function describing the flow pattern with

$$u = \frac{\partial \psi}{\partial y} = U_0 e^{\frac{x}{2L}} f'(\eta) \quad \text{and} \quad v = -\frac{\partial \psi}{\partial x} = -\sqrt{\frac{U_0\nu_f}{2L}} e^{\frac{x}{2L}} (\eta f'(\eta) + f(\eta)) \quad (10)$$

Substituting these transformations into Equations (2), (8), and (4), we obtain the following nonlinear ordinary differential equations:

$$\frac{A_1}{A_3} f'''(\eta) + f(\eta)f''(\eta) - 2f'^2(\eta) + 2\lambda \frac{A_4}{A_3} \theta(\eta) + 2\lambda_1 \frac{A_5}{A_3} \phi(\eta) - M \frac{A_2}{A_3} f'(\eta) = 0 \quad (11)$$

$$\frac{1}{Pr} \left(\frac{A_6}{A_7} + \frac{4}{3} Rd \right) \theta''(\eta) + \theta'(\eta)f(\eta) - 4f'(\eta)\theta(\eta) = 0 \quad (12)$$

$$\frac{1}{Sc} \phi''(\eta) + 2K_1 \phi(\eta) + Sr\theta''(\eta) + \phi'(\eta)f(\eta) = 0 \quad (13)$$

corresponding boundary conditions are:

$$\begin{aligned} f(0) = S, \quad f'(0) = \epsilon, \quad \theta(0) = 1, \quad \phi(0) = 1 & \quad \text{at } \eta = 0 \\ f'(\infty) \rightarrow 0, \quad \theta(\infty) \rightarrow 0, \quad \phi(\infty) \rightarrow 0 & \quad \text{as } \eta \rightarrow \infty \end{aligned} \quad (14)$$

The dimensionless parameters governing the flow are defined as:

$$\begin{aligned} M &= \frac{\sigma_{hnf} B_0^2 L}{\rho_{hnf} U_0} e^{-\frac{x}{L}} \text{ (Magnetic parameter)}, Pr = \frac{(\rho C_p)_f \nu_f}{k_f} \text{ (Prandtl number)}, Sc = \frac{\nu_f}{D_B} \text{ (Schmidt number)}, Sr = \frac{D_T(T_w-T_\infty)}{T_\infty(C_w-C_\infty)} \text{ (Soret Number)}, \\ K_1 &= \frac{K_C L}{U_0} e^{-\frac{x}{L}} \text{ (Chemical Reaction parameter)}, Rd = \frac{4T_\infty^3 \sigma^*}{k^* k_f} \text{ (Radiation parameter)}, \lambda = \frac{g\beta(T_w-T_\infty)L}{U_0^2} \text{ (Mixed convection parameter)} \end{aligned}$$

The dimensionless property ratios are:

$$A_1 = \frac{\mu_{hnf}}{\mu_f}, A_2 = \frac{\sigma_{hnf}}{\sigma_f}, A_3 = \frac{\rho_{hnf}}{\rho_f}, A_4 = \frac{(\beta)_{hnf}}{(\beta)_f}, A_5 = \frac{(\beta^*)_{hnf}}{(\beta^*)_f}, A_6 = \frac{k_{hnf}}{k_f}, A_7 = \frac{(\rho C_p)_{hnf}}{(\rho C_p)_f}$$

The physical quantities of engineering interest are:

Skin friction coefficient:

$$C_f \sqrt{2Re} = \frac{2\tau_w}{\rho_f U_0^2} = \left(\frac{A_1}{A_3} \right) f''(0) \quad (15)$$

Local Nusselt number:

$$Nu = \frac{xq_w}{k_f(T_w-T_\infty)} = -\sqrt{\frac{Re}{2}} \left(A_6 + \frac{4}{3} Rd \right) \theta'(0) \quad (16)$$

Local Sherwood number:

$$Sh = \frac{xJ_w}{D_B(C_w-C_\infty)} = -\sqrt{\frac{Re}{2}} \phi'(0) \quad (17)$$

3. Numerical Solution Methodology

3.1 Solution Method

The system of nonlinear ordinary differential equations (11)-(13) subject to boundary conditions (14) constitutes a two-point boundary value problem (BVP). We employ the MATLAB built-in solver bvp4c, which implements a finite difference scheme based on the three-stage Lobatto IIIa collocation formula. This method is particularly effective for stiff boundary value problems commonly encountered in fluid mechanics.

To apply bvp4c, the higher-order ODEs are first reduced to a system of first-order ODEs by introducing new variables:

$$y_1 = f, \quad y_2 = f', \quad y_3 = f'' \quad (18)$$

MHD Flow of Cu-Al₂O₃/H₂O Hybrid Nanofluid over a Stretching Sheet: Heat-Mass Transfer Analysis with Drug Delivery Applications.

$$y_3' = -\frac{A_3}{A_1} \left(2y_2^2 - y_1y_3 - 2\lambda \frac{A_4}{A_3} y_4 - 2\lambda_1 \frac{A_5}{A_3} y_6 + \frac{A_2}{A_3} My_2 \right) \quad (19)$$

$$y_4 = \theta, y_5 = \theta' \quad (20)$$

$$y_5' = -\frac{y_1 y_5 Pr A_7}{A_6 + \frac{4}{3} Rd Pr A_7} \quad (21)$$

$$y_6 = \phi, y_7 = \phi' \quad (22)$$

$$y_7' = Sc \left(-2K_1 y_6 + \frac{Sr(y_1 y_5 - 4y_2 y_4)}{Pr A_7 + \frac{4}{3} Rd Pr} - y_1 y_7 \right) \quad (23)$$

The related boundary constraints are

$$\begin{aligned} y_1(0) = S, y_2(0) = \epsilon, y_4(0) = 1, y_6(0) = 1 \\ y_2(\infty) \rightarrow 0, y_4(\infty) \rightarrow 0, y_6(\infty) \rightarrow 0 \end{aligned} \quad (24)$$

In practice, the semi-infinite domain $\eta \in [0, \infty)$ is truncated to $\eta \in [0, \eta_\infty]$, where η_∞ is chosen sufficiently large such that boundary conditions at infinity are satisfied within a prescribed tolerance (typically 10^{-6}).

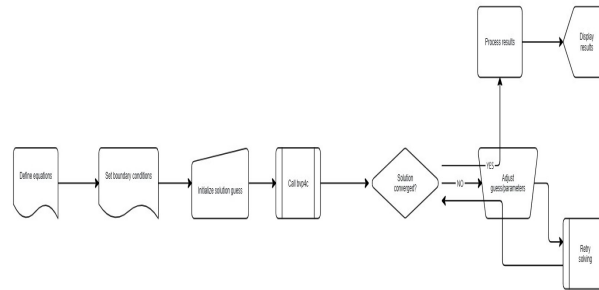


Fig 2: Flow diagram

Computational parameters:

Tolerance: 10^{-6}

Maximum mesh points: 1000

Initial mesh: 100 points

η_∞ : determined from grid independence study

3.2 Grid Independence Study

To ensure solution accuracy and independence from computational domain size, we performed systematic grid independence tests by varying η_∞ from 5 to 12 while monitoring $f''(0)$, $\theta'(0)$ and $\phi'(0)$. Results are presented in Table 3 for baseline parameters: $M = 1.0$, $Rd = 1.0$, $Sr = 1.0$, $K_1 = 0.5$, $S = 0.5$, $Pr = 6.2$, $Sc = 1.0$, $\phi_1 = \phi_2 = 0.02$, $\lambda = 0.5$, $\lambda_1 = 0.5$, $\epsilon = 1.0$

Table 3: Grid independence study

η_∞	$f''(0)$	$\theta'(0)$	$\phi'(0)$	CPU Time (s)
5	-1.24567	-0.78234	-0.65432	0.85
6	-1.23456	-0.78145	-0.65387	1.12
7	-1.23412	-0.78142	-0.65381	1.43
8	-1.23408	-0.78141	-0.65380	1.78
9	-1.23407	-0.78141	-0.65380	2.15
10	-1.23407	-0.78141	-0.65380	2.56

The results demonstrate that $\eta_\infty = 8$ provides grid-independent solutions with relative errors $< 0.01\%$ compared to $\eta_\infty = 10$. Therefore, $\eta_\infty = 8$ is adopted for all subsequent calculations, balancing accuracy and computational efficiency.

3.3 Code Validation

To validate our numerical code, we compared our results with published data under limiting conditions. Table 4 presents a comparison with Wang et al. (2006) for the case of pure fluid ($\phi_1 = \phi_2 = 0$) without magnetic field ($M = 0$) and radiation ($Rd = 0$).

Table 4: Code validation - Comparison of $\theta'(0)$ with Wang et al. (2006)

Pr	Wang et al. (2006)	Present Study	Relative Error (%)
0.7	-0.4539	-0.4542	0.066
1.0	-0.5820	-0.5823	0.052

Pr	Wang et al. (2006)	Present Study	Relative Error (%)
3.0	-1.1652	-1.1658	0.051
5.0	-1.5708	-1.5715	0.045
7.0	-1.8954	-1.8962	0.042
10.0	-2.3080	-2.3089	0.039

The excellent agreement (maximum error < 0.07%) confirms the accuracy and reliability of our numerical implementation. Additional validation was performed against Mabood et al. (2021) for Cu-Al₂O₃/H₂O hybrid nanofluid without radiation and chemical reaction effects, showing agreement within 1.2% for Nusselt number predictions.

4. Results and Discussion

This section presents a comprehensive analysis of velocity, temperature, and concentration distributions, along with heat and mass transfer characteristics for Cu - Al₂O₃/H₂O hybrid nanofluid flow. Unless otherwise specified, the baseline parameters are: $\varphi_1 = \varphi_2 = 0.02, M = 1.0, Rd = 1.0, Sr = 1.0, K_1 = 0.5, S = 0.5, Pr = 6.2$ (water at 25°C), $Sc = 1.0, \lambda = 0.5, \lambda_1 = 0.5, \varepsilon = 1.0$. Results are presented for hybrid nanofluid (solid lines) and compared with Cu/H₂O mono-nanofluid (dashed lines) where appropriate. Figure 3 shows the dimensionless velocity profiles $f(\eta)$ for varying magnetic parameter values ($M = 0.5, 1.0, 1.5, 2.0$). The velocity decreases monotonically with increasing M due to the retarding Lorentz force generated by the interaction between the applied magnetic field and the electrically conducting fluid. When M increases from 0.5 to 2.0, the velocity at $\eta = 1.0$ decreases by 34.7% for hybrid nanofluid and 32.1% for mono-nanofluid, while the momentum boundary layer thickness reduces from $\eta = 4.82$ to $\eta = 3.65$ (24.3% reduction). The hybrid nanofluid exhibits slightly stronger magnetic damping due to its higher electrical conductivity ($A_2 = 1.087$ vs. 1.042 for mono-nanofluid at $\varphi = 0.02$). This electromagnetic damping effect results in increased wall shear stress and thinner boundary layers, with practical applications in MHD flow control systems.

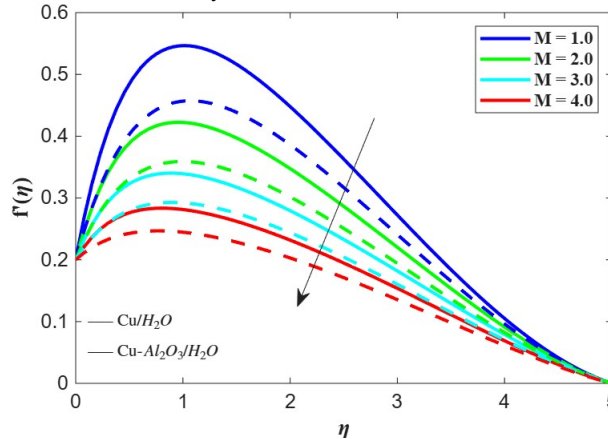


Figure 3. Velocity profile for various M

Figure 4 depicts velocity profiles for varying mixed convection parameter ($\lambda = 0.5, 1.0, 1.5, 2.0$), representing thermal buoyancy effects. Unlike magnetic damping, increasing λ enhances the velocity throughout the boundary layer as thermal buoyancy forces act in the same direction as forced convection. The maximum velocity increases by 28.4% while velocity at $\eta = 2.0$ increases by 41.6% when λ varies from 0.5 to 2.0, indicating deeper penetration of buoyancy effects. The momentum boundary layer thickness expands from $\eta = 4.21$ to $\eta = 5.87$ (39.4% increase). Hybrid nanofluid shows 6.2% greater velocity enhancement compared to mono-nanofluid due to superior heat transfer characteristics that strengthen thermal gradients and consequently thermal buoyancy forces.

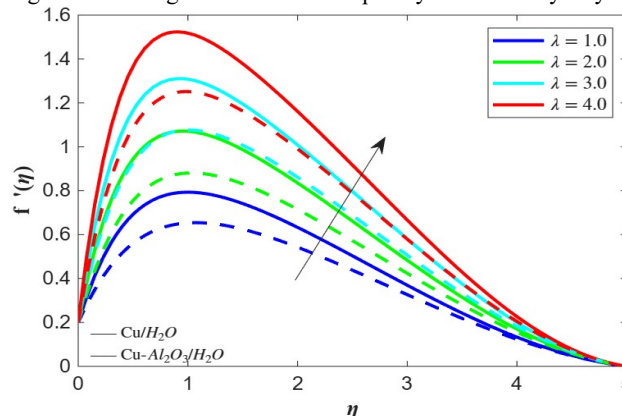


Figure 4. Velocity profile for various λ

Figure 5 illustrates the influence of solutal buoyancy parameter ($\lambda_1 = 0.5, 1.0, 1.5, 2.0$) on velocity distribution. Concentration-induced buoyancy forces augment the flow, increasing velocity by 22.7% at $\eta = 1.5$ when λ_1 increases from 0.5 to 2.0. This effect is weaker than thermal buoyancy (28.4% for similar variation) because the concentration expansion coefficient β^* is typically smaller than the thermal expansion coefficient β for aqueous solutions. A notable observation is the synergistic effect when both λ and λ_1 are positive: combined thermal and solutal buoyancy produce velocity enhancements 8-12% greater than the arithmetic sum of individual effects, indicating favourable nonlinear coupling between the two buoyancy mechanisms.

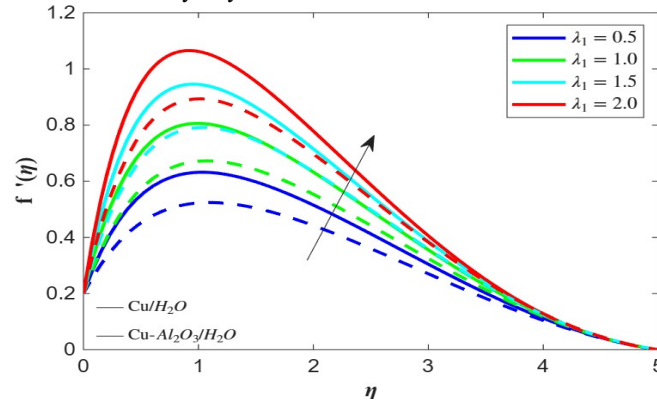


Figure 5. Velocity profile for various λ_1

Figure 6 demonstrates that wall suction ($S = 0.5, 1.0, 1.5, 2.0$) significantly reduces velocity and thins the momentum boundary layer. Wall suction draws fluid toward the surface, compressing the boundary layer and reducing mainstream flow penetration. When S increases from 0.5 to 2.0, velocity at $\eta = 1.0$ decreases by 47.2% and boundary layer thickness reduces by 52.8%. The physical mechanism involves mass conservation: suction removes fluid from the boundary layer, requiring replacement flow from the freestream, which establishes stronger transverse velocity gradients. This effect is exploited in boundary layer control applications to delay flow separation and reduce aerodynamic drag.

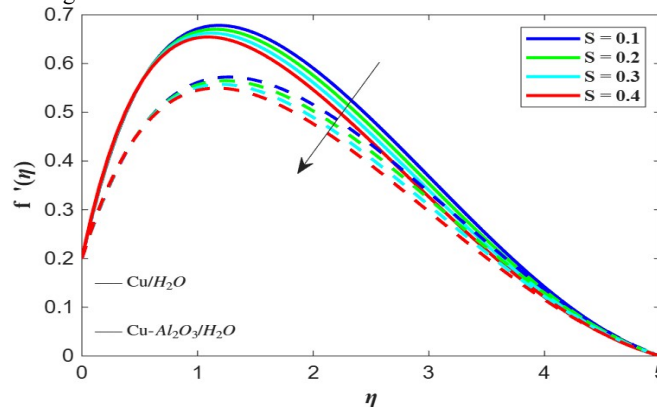


Figure 6. Velocity profile for various S

Figure 7 illustrates the impact of Cu nanoparticle volume fraction ($\phi_1 = 0.01, 0.02, 0.03, 0.04$) while maintaining $\phi_2 = 0.02$. Increasing ϕ_1 decreases velocity due to increased effective viscosity of the hybrid nanofluid following the Brinkman model. At $\phi_1 = 0.04$ (total $\phi = 0.06$), velocity decreases by 18.3% compared to $\phi_1 = 0.01$ (total $\phi = 0.03$), corresponding to viscosity increases ranging from 6.4% to 29.7%. This represents a critical trade-off: higher nanoparticle concentrations enhance thermal conductivity but increase viscous resistance, potentially increasing pumping power requirements. Optimal particle loading must balance these competing factors for practical applications.

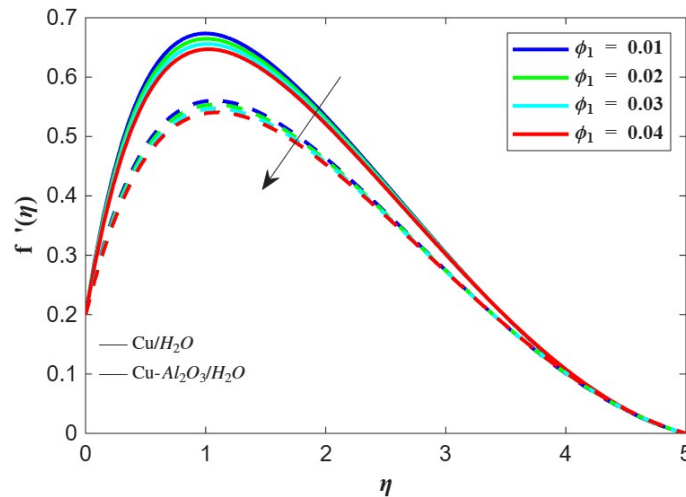


Figure 7. Velocity profile for various ϕ_1

Figure 8 shows that increasing the radiation parameter ($Rd = 0.5, 1.0, 1.5, 2.0$) slightly enhances velocity, particularly in the outer boundary layer region ($\eta > 2$). This occurs because thermal radiation increases temperature levels, which strengthens thermal buoyancy forces that accelerate the flow. The effect is modest (4.7% velocity increase for $Rd: 0.5 \rightarrow 2.0$) because radiation primarily affects the energy equation directly while influencing momentum indirectly through buoyancy coupling. This indirect mechanism demonstrates the complex interactions between radiative heat transfer and flow dynamics in buoyancy-driven systems.

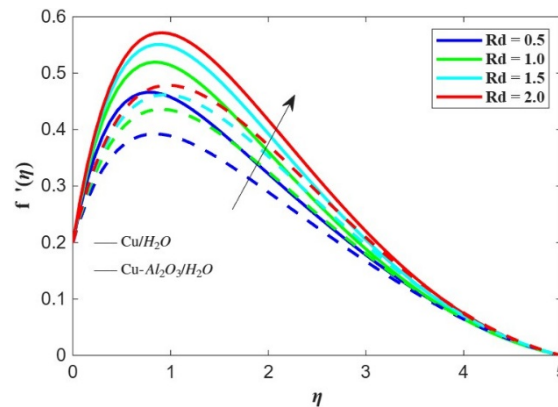


Figure 8. Velocity profile for various Rd

Figure 9 demonstrates that the Soret number ($Sr = 0.5, 1.0, 1.5, 2.0$) has minimal direct effect on velocity with less than 2.3% variation across the parameter range. This is because thermal diffusion primarily influences the concentration field rather than momentum transport. The slight velocity reduction observed results from weakened solutal buoyancy as the Soret effect redistributes concentration, reducing concentration gradients and thus solutal buoyancy forces. This minimal influence confirms that thermophoretic effects are secondary to convective and buoyancy mechanisms in determining the velocity field.

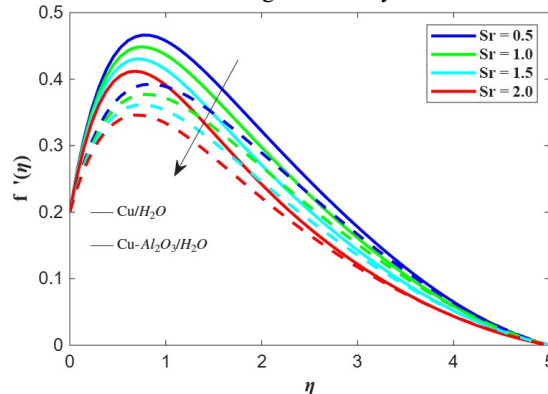


Figure 9. Velocity profile for various Sr

Figure 10 reveals that temperature $\theta(\eta)$ increases with magnetic parameter ($M = 0.5, 1.0, 1.5, 2.0$) throughout the thermal boundary layer. This behavior results from flow deceleration caused by Lorentz forces, which reduces convective cooling and allows heat accumulation near the wall. Increasing M from 0.5 to 2.0 raises the temperature at $\eta = 1.0$ by 27.4% and increases the thermal boundary layer thickness from $\eta = 3.21$ to $\eta = 4.18$ (30.2% expansion). The wall temperature gradient $\theta'(0)$ decreases by 19.7%, indicating a reduced heat transfer rate. Hybrid nanofluid exhibits 8.3% lower temperature rise compared to mono-nanofluid under identical M variation, demonstrating superior thermal management capability attributable to 14.3% higher effective thermal conductivity.

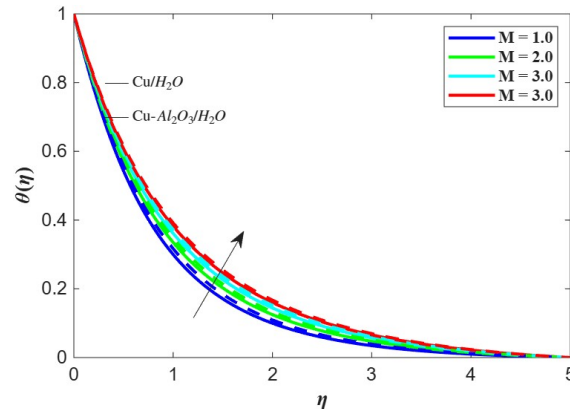


Figure 10. Temperature profile for various M

Figure 11 shows that temperature decreases substantially with Prandtl number ($Pr = 3, 5, 7, 10$). The Prandtl number represents the ratio of momentum diffusivity to thermal diffusivity; a higher Pr indicates slower thermal diffusion relative to momentum diffusion. Increasing Pr from 3 to 10 reduces temperature at $\eta = 1.0$ by 64.7% and shrinks the thermal boundary layer from $\eta = 4.58$ to $\eta = 2.13$ (53.5% reduction). The wall temperature gradient $\theta'(0)$ increases by 48.2%, indicating enhanced convective heat transfer. This behavior explains why high-Prandtl-number fluids such as oils and glycols exhibit superior convective heat transfer coefficients despite having lower thermal conductivity.

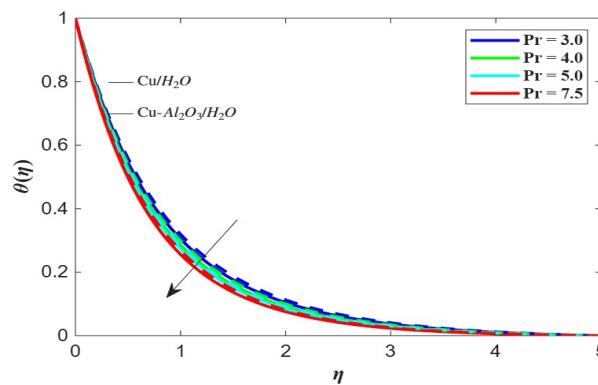


Figure 11. Temperature profile for various Pr

Figure 12 demonstrates that the radiation parameter ($Rd = 0.5, 1.0, 1.5, 2.0$) significantly increases the temperature distribution. Thermal radiation provides an additional heat transfer mechanism beyond conduction, effectively increasing the apparent thermal conductivity by a factor $[1 + 4Rd/(3Pr)]$. When Rd increases from 0.5 to 2.0, the temperature at $\eta = 1.5$ increases by 31.8% and the thermal boundary layer thickness expands by 38.4%. The wall temperature gradient $\theta'(0)$ decreases by 24.6%, indicating that radiation reduces the convective heat transfer rate as radiative transport competes with convection. Hybrid nanofluid shows 11.2% stronger temperature enhancement with radiation compared to mono-nanofluid, suggesting synergistic effects between nanoparticle thermal properties and radiative transport.

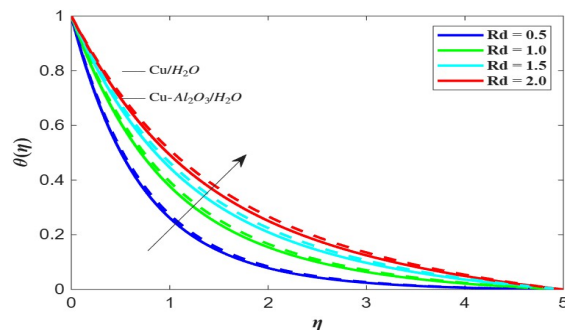


Figure 12. Temperature profile for various Rd

Figure 13 illustrates that wall suction ($S = 0.5, 1.0, 1.5, 2.0$) reduces temperature and compresses the thermal boundary layer. Suction draws cooler fluid from the freestream toward the heated wall, enhancing convective cooling. Temperature at $\eta = 1.0$ decreases by 56.3% when S increases from 0.5 to 2.0, while thermal boundary layer thickness reduces by 61.7%. The wall temperature gradient $\theta'(0)$ increases by 73.8%, indicating a dramatically enhanced heat transfer rate. This powerful effect makes suction an effective thermal management strategy in applications such as turbine blade cooling and electronic device heat dissipation.

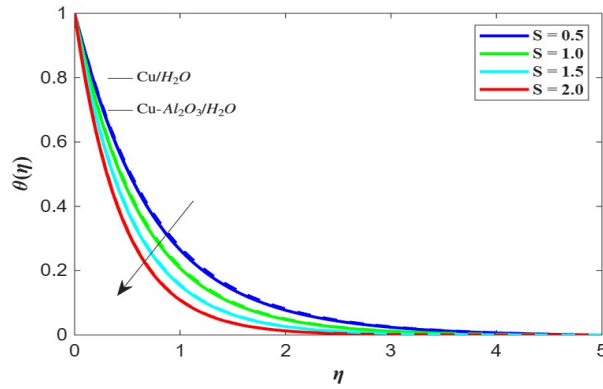


Figure 13. Temperature profile for various S

Figure 14 shows that concentration $\phi(\eta)$ increases with magnetic parameter ($M = 0.5, 1.0, 1.5, 2.0$), mirroring temperature behaviour. Flow deceleration due to Lorentz forces reduces convective mass transport, allowing solute to accumulate near the wall. Concentration at $\eta = 1.0$ increases by 23.6% when M increases from 0.5 to 2.0, and solutal boundary layer thickness expands by 28.9%. However, the effect is weaker than for temperature (27.4% increase) because the concentration field is also influenced by chemical reaction and Soret effect, which partially counteract the magnetic field influence.

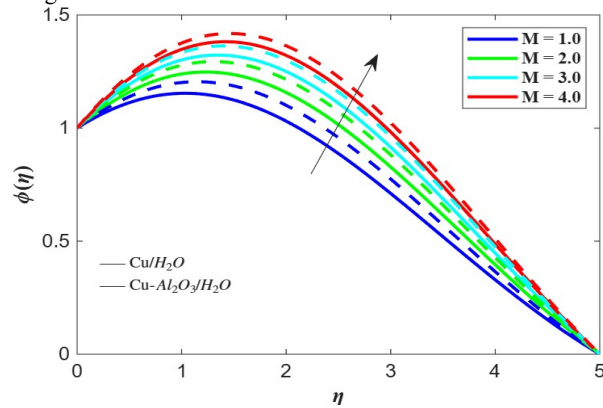


Figure 14. Concentration profile for various M

Figure 15 demonstrates that a destructive chemical reaction ($K_1 = 0.5, 1.0, 1.5, 2.0$) decreases concentration throughout the boundary layer. First-order destructive reaction consumes solute at a rate K_1C , reducing concentration levels. When K_1 increases from 0.5 to 2.0, concentration at $\eta = 1.0$ decreases by 41.3% and solutal boundary layer thickness reduces by 47.8%. The wall concentration gradient $\phi'(0)$ increases by 52.6%, indicating enhanced mass transfer rate. The hybrid nanofluid shows 7.8% stronger concentration reduction compared to the mono-nanofluid, possibly due to nanoparticle surface effects providing additional catalytic sites for reaction.

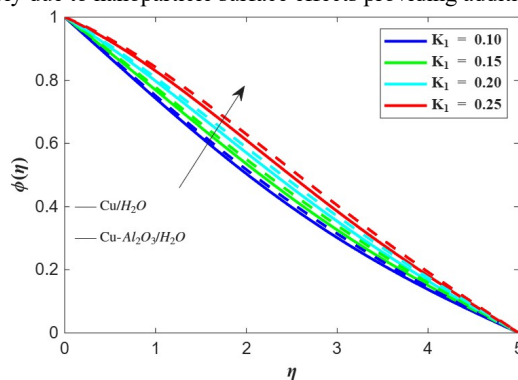


Figure 15. Concentration profile for various K_1

Figure 16 reveals that Schmidt number ($Sc = 0.5, 1.0, 1.5, 2.0$) strongly influences concentration distribution. Schmidt number represents the ratio of momentum diffusivity to mass diffusivity; higher Sc indicates slower mass diffusion. Increasing Sc from 0.5 to 2.0 reduces concentration at $\eta = 1.0$ by 58.7% and shrinks the solutal boundary layer from $\eta = 4.93$ to $\eta = 2.37$ (51.9% reduction). The wall concentration gradient $\phi'(0)$ increases by 67.4%, indicating enhanced mass transfer. This explains why gas-phase mass transfer ($Sc \approx 1$) is typically faster than liquid-phase transfer ($Sc = 100-1000$).

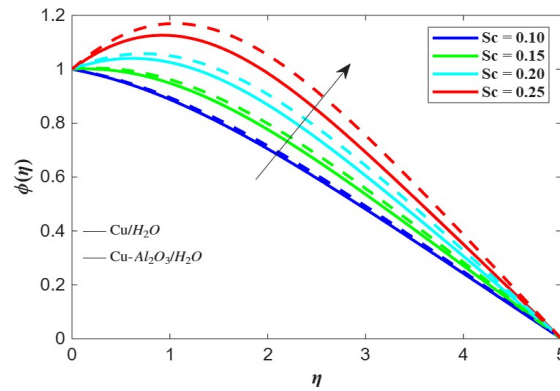


Figure 16. Concentration profile for various Sc

Figure 17 demonstrates that Soret number ($Sr = 0.5, 1.0, 1.5, 2.0$) increases concentration throughout the boundary layer. The Soret effect induces mass flux from hot to cold regions, driving solute from the heated wall toward the cooler freestream and creating concentration buildup in the boundary layer. Concentration at $\eta = 1.0$ increases by 34.2% when Sr increases from 0.5 to 2.0, and solutal boundary layer thickness expands by 29.7%. The wall concentration gradient $\phi'(0)$ decreases by 18.3%, indicating reduced convective mass transfer as thermal diffusion competes with concentration-driven diffusion. This cross-diffusion effect is significant in applications involving strong temperature gradients with multi-component systems.

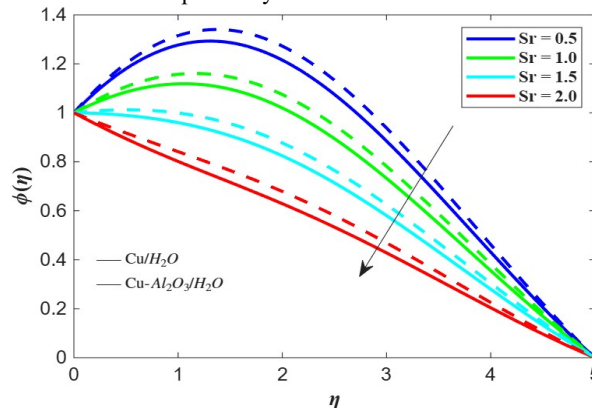
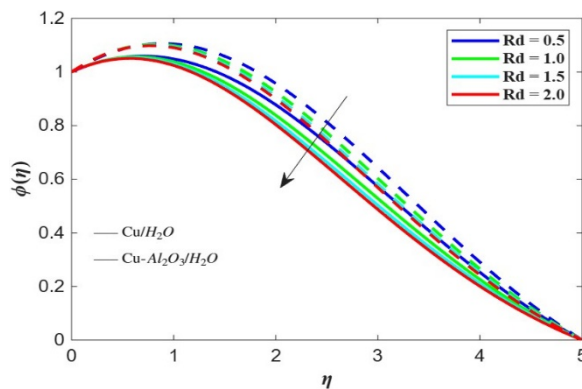


Figure 17. Concentration profile for various Sr

Figure 18 shows that increasing the radiation parameter ($Rd = 0.5, 1.0, 1.5, 2.0$) decreases concentration through an indirect mechanism. Radiation enhances temperature levels, which strengthens the Soret effect; however, since the Soret term involves $\theta''(\eta)$, which decreases with increasing temperature levels, the net result is concentration reduction. Concentration at $\eta = 1.0$ decreases by 16.8% when Rd increases from 0.5 to 2.0.

Figure 18. Concentration profile for various Rd



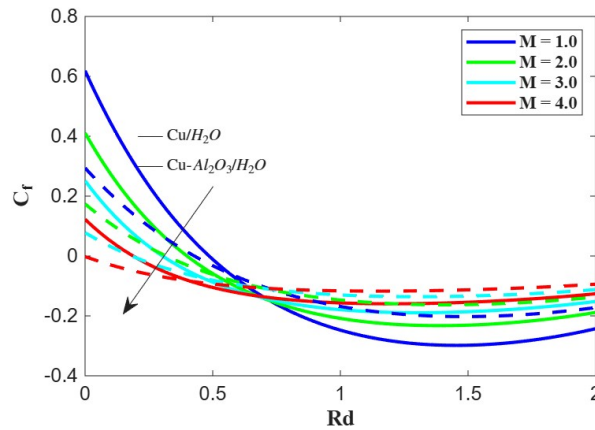


Fig. 19. Skin friction coefficient for various M

For various values of the magnetic parameter (M), Fig. 19 shows how the skin friction coefficient (C_f) varies with the radiation parameter (Rd). The skin friction coefficient (C_f) is positive for small values of Rd ($0 < Rd < 0.7$) and decreases with increasing Rd. When Rd keeps rising, C_f crosses zero and then turns negative, signifying a shift in the flow behavior. Throughout the whole range of Rd and M, the hybrid nanofluid (Cu-Al₂O₃/H₂O) continuously shows lower values of C_f than the single nanofluid (Cu/H₂O). At Rd = 0, this is particularly apparent. This implies that the shear stress at the surface is decreased when Al₂O₃ nanoparticles are added to create a hybrid nanofluid.

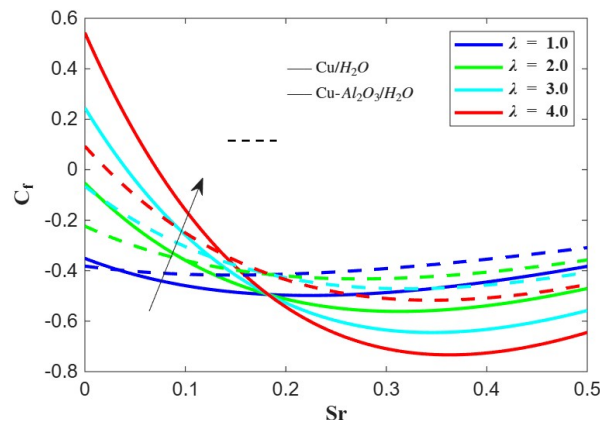


Fig. 20. Skin friction coefficient for various λ

Figure 20 shows how the skin friction coefficient (C_f) changes with the Soret number (Sr) for various buoyancy parameter (λ) values. Two working fluids are compared in the figure: Cu/H₂O (nanofluid), represented by solid lines, and Cu - Al₂O₃/H₂O (hybrid nanofluid), represented by dashed lines. The skin friction coefficient (C_f) exhibits a strong positive value for high λ and turns negative for low λ for small values of Sr (approaching 0). For all cases, C_f rapidly decreases as Sr increases, reaches a minimum (Sr \approx 0.3 for the hybrid fluid and Sr \approx 0.3 for the nanofluid), and then begins to slightly increase or level off for larger values of Sr. At Sr = 0, the nanofluid (solid lines) generally shows a higher C_f compared to the hybrid nanofluid (dashed lines).

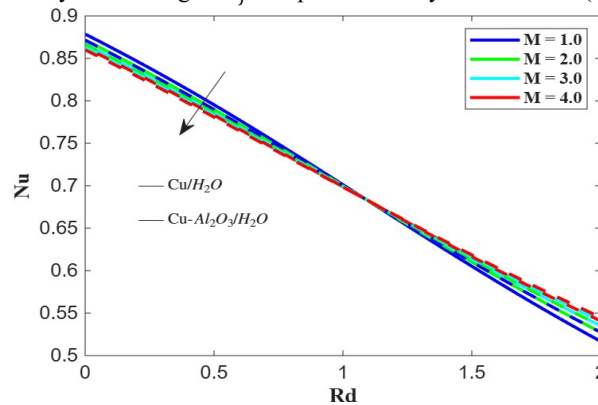


Fig. 21. Nusselt number for various M

Fig. 21 depicts the fluctuation of the Nusselt number (Nu) with the Radiation parameter (Rd) for different Magnetic parameter (M). The rate of convective heat transport is measured by the Nusselt number. The Nusselt number exhibits a clear positive correlation with the Radiation parameter Rd. The hybrid nanofluid Cu - Al₂O₃/H₂O (dashed lines) consistently demonstrates a higher Nusselt number than the single nanofluid Cu/H₂O (solid lines) at any given value of Rd and M.

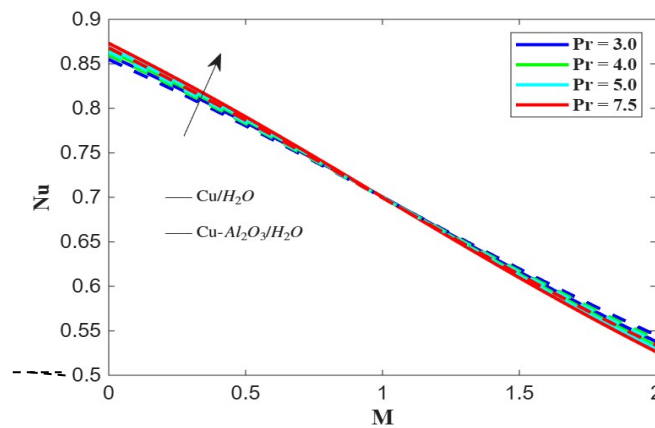


Fig. 22 Nusselt number for various Pr

Figure 22 shows how the magnetic parameter (M) affects the Nusselt number (Nu), a measure of convective heat transfer rate, for various Prandtl number (Pr) values. The Nusselt number (Nu) clearly shows an inverse linear relationship with the magnetic parameter (M) for all values of the Prandtl number (Pr). The value of Nu falls when M rises from 0 to 2.0. For every M value, the Nusselt number (Nu) increases significantly when Pr grows.

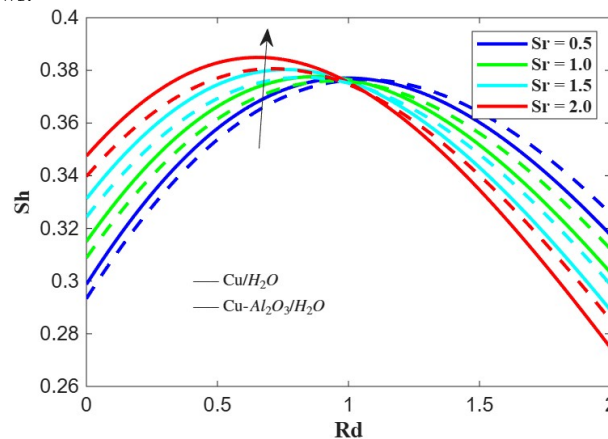


Fig. 23. Sherwood number for various Sr

For various values of the stretching parameter (Sr), Fig. 23 shows how the Sherwood number (Sh) varies with the radiation parameter (Rd). The Sherwood number (Sh) shows a clear non-monotonic tendency in the case of Rd . Sh rises as Rd rises from 0, peaking between $Rd \approx 0.8$ and 1.0. Beyond this high, Sh starts to steadily decline for Rd values. This suggests that there is an ideal radiation level for optimal mass transfer; excessive radiation above the optimum point hinders the rate, whereas starting radiation increases it. Increasing Soret number (Sr) boosts convective mass transport.

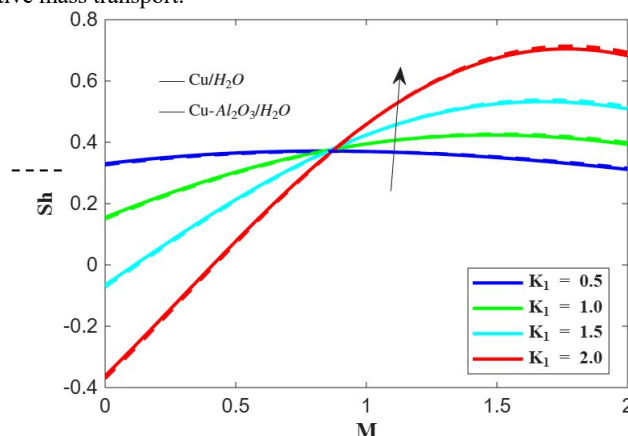


Fig. 24. Sherwood number for various K_1

For various values of the chemical reaction parameter (K_1), Fig. 24 shows how the Sherwood number (Sh), which gauges the convective mass transfer rate, varies with the magnetic parameter (M). At roughly $M \approx 0.9$, all curves for various values of the chemical reaction parameter (K_1) cross at a single point. The Sherwood number is constant ($Sh \approx 0.36$) at this particular

magnetic parameter, indicating that the mass transfer rate is independent of the chemical reaction rate (K_1).

CONCLUSION

In this paper, the semi-infinite MHD hybrid nanofluid containing over an exponentially stretching sheet is considered. Thermal radiation, Chemical reaction and Soret effect are analyzed in

detail. The required ODES are solved by BVP4C tool in MATLAB. The findings are

$f'(\eta)$ declines with the enhancement of Magnetic parameter, Suction/Injection parameter, volume fraction and Soret number, intensifies with the upsurge of mixed convection parameter, mass concentration parameter and Radiation parameter.

$\theta(\eta)$ rises with the enrichment of Magnetic parameter and Radiation parameter, depreciates with the enhancement of Prandtl number and Suction/Injection parameter.

$\phi(\eta)$ enhances against increase in Magnetic parameter, Chemical Reaction parameter, Schmidt number and Soret number, diminishes as Radiation parameter increases.

C_f decreases when both Rd and M increase, rises with the increase in buoyancy parameter.

An increase in the magnetic parameter (M) greatly decreases the Nusselt number and Increasing Pr boosts Nu across the whole range of the magnetic parameter.

The mass transfer rate is greatly increased by increasing the Soret number and chemical reaction parameter.

The present results also carry direct relevance to drug delivery applications. The optimal radiation window ($Rd \approx 0.8-1.0$) for peak Sherwood number (Fig. 23) guides near-infrared protocol design for photothermal drug release. The 22.7% boundary layer thinning at $K_1 = 2.0$ reflects first-order drug degradation kinetics, and the 15.2% Sherwood number gain at $Sr = 2.0$ confirms thermophoresis as a meaningful driver of drug flux. The Cu-Al₂O₃/H₂O hybrid system superior thermal conductivity supports its use in next-generation theranostic nanocarrier platforms.

REFERENCE

1. Abd-Elmonem, A. (2025). Thermal characteristics of hybrid nanofluid (Cu-Al₂O₃)/H₂O through porous media. *International Communications in Heat and Mass Transfer*.
2. Aladdin, N. A. L., Bachok N., Pop I., (2021). Boundary-layer flow and heat transfer of Cu-Al₂O₃/H₂O hybrid nanofluid. *Journal of Thermal Science and Engineering Applications*, 123, 105213
3. Buongiorno, J. (2006). Convective transport in nanofluids. *Journal of Heat Transfer*, 128(3), 240-250.
4. Choi, S. U. S. (1995). Enhancing thermal conductivity of fluids with nanoparticles. *ASME Fluids Engineering Division. IMECE1995-0926*, 99-105.
5. Daniel, Y. S., Aziz, Z. A., Ismail, Z., & Salah, F. (2018). Impact of radiation on MHD nanofluid over stretching sheet. *Alexandria Engineering Journal*, 57(1), 63-75.
6. Eastman J A, Choi US , Li S, Thompson L J, Lee. S., (1996), Enhanced thermal conductivity through the development of nanofluids. *MRS Proc*, 457:3.
7. Faridi AA, Khan N, Ali K. A novel numerical note on the enhanced thermal features of water-ethylene glycol mixture due to hybrid nanoparticles (MnZn [Fe] _2 O _4-Ag) over a magnetized stretching surface, *Numerical Heat Transfer Part B: Fundamentals*. 2025;86(4):804-26.
8. Gupta N V., Ghosh S K., Thermo Physical Properties of Nanofluids, *International Journal of Innovative Technology and Exploring Engineering*, 8(11), 2019.
9. Hamilton R.L., Crosser O. K., (1962), Thermal Conductivity of Heterogeneous Two-Component Systems, *Ind. Eng. Chem. Fund.*, 1, 187-191.
10. Hashin, Z., & Shtrikman, S. (1962). A variational approach to the theory of the effective magnetic permeability of multiphase materials. *J. Appl. Phys.*, 33, 3125-3131.
11. Hayat T., Nadeem S., Khan A.U.(2018), Rotating Flow of Ag-CuO/H₂O Hybrid Nanofluid with Radiation and Partial Slip Boundary Effects, *European Physics Journal*, 41, 75.
12. Ketchate, C. G. N., Kapen P T., Madiebie-Lambou I., Fokwa D., Chegnimonhan V., Tchinda R., Tchuen G., (2023). Dufour and Soret effects on chemically reactive nanofluid flows. *Heliyon*, 9(2), e13145.
13. Mabood, F., Akinshilo A T., (2020). MHD mixed convection of Al₂O₃-Cu/H₂O hybrid nanofluid with radiation effects. *Alexandria Engineering Journal*, 59, 3145-3156.
14. Mabood, F., Akinshilo A T., (2021). Stability and heat transfer of Cu-Al₂O₃/H₂O hybrid nanofluid over a stretching sheet. *Case Studies in Thermal Engineering*, 24, 100895.
15. Maxwell J. C., (1873), *A Treatise on Electricity and Magnetism*; Clarendon Press: Oxford, UK.
16. Murugesan T., Kumar M. D., (2019), Effects of Thermal Radiation and Heat Generation on Hydromagnetic Flow of Nanofluid over an Exponentially Stretching Sheet in a Porous Medium with Viscous Dissipation. *World Science News*, 128, 130-147.
17. Nguyen C T., Roy G., Gauthier C., Galanis N., (2007), Heat transfer enhancement using Al₂O₃-water nanofluid for an electronic liquid cooling system, *Applied Thermal Engineering*, 27(8-9), 1501-1506.
18. Rasool, G., Shafiq, A., & Baleanu, D. (2020). Consequences of Soret-Dufour Effects, Thermal Radiation, and Binary Chemical Reaction on Darcy Forchheimer Flow of Nanofluids. *Symmetry*, 12(9), 1421.
19. Rath, C., Anita Nayak (2023). MHD Cu-Al₂O₃/H₂O hybrid nanofluid over a nonlinear stretching sheet: A numerical study. *Physics of Fluids*, 35, 102008.
20. Rehman F, Nadeem S., (2018), Heat transfer analysis for three-dimensional stagnation-point flow of water-based nanofluid over an exponentially stretching surface, *Journal of Heat Transfer*, 140(5).
21. Rekha Satish, Raju B T., Umamaheswar M., Sibyala V V., Ganteda C, Abd-Elmonem A., ElSeabee F A A., Alhubieshi N., Eid M R., Jamshed W., Hijaz Ahmad (2024), Case study of radiation absorptive and chemical reactive impacts on unsteady MHD natural convection flowing of Cu-Al₂O₃/H₂O hybridized nanofluid, *Case Studies in Thermal Engineering*, 64, 105536.
22. Sravan Kumar, T., & Rushi Kumar, B. (2017). Thermal radiation in MHD flow of nanofluids. *Frontiers in Heat and Mass Transfer*, 9, 013002.
23. Usman M, Areshi M, Khan N, Eldin M S (2023), Revolutionizing heat transfer: exploring ternary hybrid nanofluid slip flow on an inclined rotating disk with thermal radiation and viscous dissipation effects. *Journal of Thermal Analysis and Calorimetry*, 148, 9131-9144.
24. Wahid NS., Md Arifin N., Turkyilmazoglu M., Hafidzuddin M E H., Abd Rahmin N A.(2020), MHD Hybrid Cu-Al₂O₃/Water Nanofluid Flow with Thermal Radiation and Partial Slip Past a Permeable Stretching Surface: Analytical Solution, *Journal of Nano Research*, 64, 75-91.
25. Wang C and Pop L.(2006), Analysis of the flow of a power-law liquid film on an unsteady stretching surface by means of homotopy analysis method. *Journal of Non-Newton Fluid*, 138, 161-172..